Earth and Planetary Science Letters 474 (2017) 20–24

Contents lists available at ScienceDirect

Earth and Planetary Science Letters

www.elsevier.com/locate/epsl

Surface roughness of Titan's hydrocarbon seas

Cyril Grima[a,*], Marco Mastrogiuseppe[b], Alexander G. Hayes[b], Stephen D. Wall[c], Ralph D. Lorenz[d], Jason D. Hofgartner[c], Bryan Stiles[c], Charles Elachi[c], The Cassini RADAR Team

[a] Institute for Geophysics, University of Texas at Austin, TX 78758, United States
[b] Cornell University, Ithaca, NY 14853, United States
[c] Jet Propulsion Laboratory, California Institute of Technology, Pasadena, CA 91109, United States
[d] The Johns Hopkins University Applied Physics Laboratory, Laurel, MD 20723, United States

ARTICLE INFO

Article history:
Received 1 September 2016
Accepted 3 June 2017
Available online 29 June 2017
Editor: C. Sotin

Keywords:
Titan
radar
roughness
waves

ABSTRACT

We derive fields of solutions for the surface properties (roughness and permittivity) of the liquid hydrocarbon bodies Ligeia, Kraken and Punga Mare on Titan by applying the Radar Statistical Reconnaissance (RSR) technique to the Cassini RADAR observations in altimeter mode during the northern early summer. At the time of observation, Kraken and Ligeia were confined within root-mean-square heights of 1.5–2.5 mm (similar to wave heights of 6–10 mm), correlation lengths of 45–115 mm, and corresponding to effective slopes of 1.1–2.4°. The latter extends up to 3.6–4.9° if the rougher Punga is included. The lower bound of those ranges has to be considered if the composition of the seas is methane-dominant. These are the first measurements to simultaneously constrain both the vertical and horizontal roughness parameters of Titan's seas from the same observations. Our results are representative for the global properties of the sea-scaled portion of the studied tracks and suggest that quiet surfaces are a dominant trend over the seas during the northern early summer. Fields of rougher textures, if existent, might develop mainly over local patches and/or might not be sustained over significant periods of time.

1. Introduction

Titan's surface bodies are similar to those on Earth, shaped by aeolian, pluvial, fluvial, lacustrine, tectonic, impact and possibly cryovolcanic processes (e.g. Aharonson et al., 2014; Poggiali et al., 2016). In that respect, investigating the properties of Titan's surface is a key to better understanding surface-atmosphere exchanges and climate dynamics. Of particular interest is dimensioning the waves (i.e. roughness when observed with signals of higher wavelength) rippling the hydrocarbon liquid bodies of the Saturnian moon. Waves can be, for example, wind-driven, ruffled by tidal flows, rain, or debris, so that their characterization can be used as a discriminator for the possible processes disturbing liquid surfaces. Ghafoor et al. (2000), Lorenz et al. (2005, 2010), Lorenz and Hayes (2012), Hayes et al. (2013). In addition, knowledge of liquid bodies' roughness is critical to the prediction of post-impact behavior for safe deployment of automatic probes (Ghafoor et al., 2000; Lorenz and Hayes, 2012).

The roughness of Titan liquid bodies have been assessed from the Cassini RADAR altimetry mode (normal incidence observations) using a classic specular model (Wye et al., 2009; Zebker et al., 2014). In this approach, the expected reflection coefficient in power for a liquid methane–ethane surface is weakened by $exp[-(4\pi\sigma_h/\lambda)^2]$, where σ_h and λ are the surface's root mean square (RMS) height (σ_h) and the signal wavelength, respectively (Bennett and Porteus, 1961). To apply this model, the effective value for the received surface echo power is implicitly considered as around-the-mean of a set of observations, of which randomness adds uncertainty to the derived surface properties. Thus, Wye et al. (2009) bounded $\sigma_h < 3$ mm from the T49 Cassini flyby over Ontario Lacus, while Zebker et al. (2014) estimated σ_h ranges from 0.5 to 1.5 mm over Ligeia Mare (T91). Non-simultaneous to radar measurements was the 0.05° upper limit for the surface slopes as derived from the specular reflection observed at 5 μm over Jingpo Lacus (T58) by the Visual and Infrared Mapping Spectrometer (VIMS) (Stephan et al., 2010; Barnes et al., 2011). Those values are consistent with a very smooth, quasi-undisturbed, surface. VIMS observations of diffused light over a localized patch within the boundaries of Punga Mare (T85) would correspond to surface slopes of 6° that could accommodate a slightly rougher liquid surface (Barnes et al., 2014). Also, The imager mode of the Cassini RADAR detected what could be local and transient rough patches at the surface of Ligeia Mare (Hofgartner et al., 2014, 2016).

* Corresponding author.
E-mail address: cyril.grima@gmail.com (C. Grima).

http://dx.doi.org/10.1016/j.epsl.2017.06.007
0012-821X/

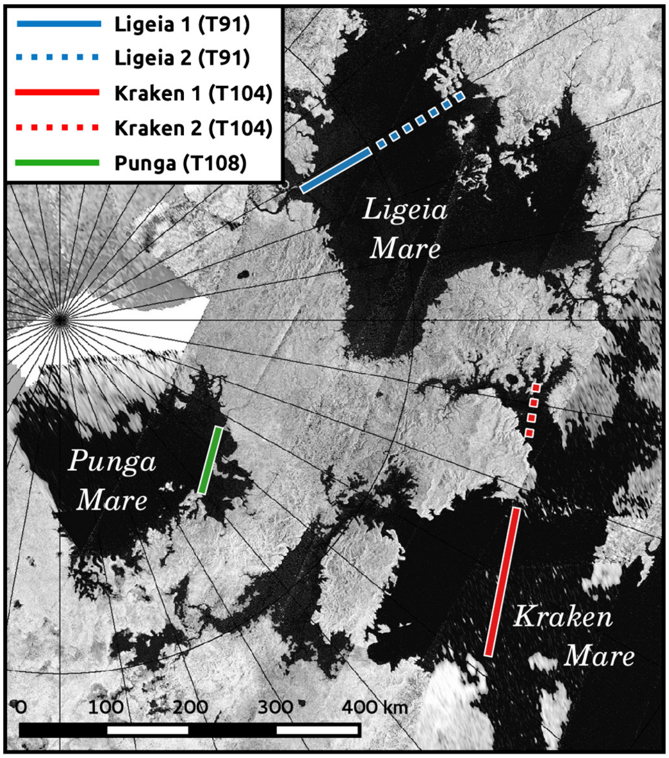

Fig. 1. Contextual map locating our regions of interest in the northern hemisphere of Titan. The background map is a Synthetic Aperture Radar mosaic of the surface from the Cassini RADAR.

The specular approach as applied by Wye et al. (2009) and Zebker et al. (2014) is valid for a coherent signal, i.e. with a deterministic phase. However, surface roughness birth and growth also causes the transfer of some coherent energy (P_c) into incoherent/random energy (P_n), the sum of both being the total received signal ($P = P_c + P_n$) (e.g. Ogilvy, 1991; Ulaby and Long, 2014). In case of the highly specular Titan's lakes, P_c is dominant by several orders of magnitude over P_n, and neglecting the latter does not have a severe impact on the derived σ_h estimates. Yet, P_n is highly sensitive to extra information regarding the roughness (Grima et al., 2014b) and its consideration, together with P_c, is an opportunity to better describes and constrains the surface properties.

In this study we apply the Radar Statistical Reconnaissance (RSR) technique (Grima et al., 2012, 2014b) to the altimetry observations from the Cassini RADAR over Ligeia (T91), Kraken (T104), and Punga (T108) seas, the three largest liquid bodies in the Northern hemisphere (Fig. 1). These observations span the first half of the Cassini Solstice mission (Northern early summer) at solar longitudes (L_S) of 45.22° (Ligeia), 59.38° (Kraken), and 63.78° (Punga). The RSR augments the classic specular model by considering the signal randomness behavior as a signature for the coherent–incoherent energy balance within the total received signal. The RSR product is a range of possible solutions for ϵ, σ_h, and the surface correlation length (l_c). We first present the dataset used along with a description of the RSR methodology and its application to the Cassini RADAR data. Then, we present the obtained surface roughness properties for the considered seas. Finally, we highlight some specifics of radar backscattering for a better understanding of the results and we discuss the implications in terms of wave generation and spatial/seasonal occurrence.

2. Data and method

The Cassini RADAR is an active 13.8 GHz ($\lambda =$ 2.2 cm) multiple-beam instrument with observation angles arranged across-track (Elachi et al., 2004; West et al., 2009). It is a part of the science payload for the NASA's Cassini spacecraft touring the Saturnian system and its moons since 2004 (Matson et al., 2002). The Cassini RADAR can operate sequentially in several modes: Radiometer (Receive-only), scatterometer (off-nadir transmission/reception), altimeter (nadir transmission/reception), and imager (synthetic aperture radar). The transmission sequence of the altimeter mode is a packet (a.k.a. burst) of ∼21 consecutive chirps at fixed rate, while about 15 of them are received back and recorded after reflection. The burst repetition frequency is adjustable to adapt to various targets and observation configurations. We used observations from the Cassini flybys where the signal is not saturated. In our analysis of these observations, we did not consider the overlapping of the burst's footprints with surrounded lands/islands. The relative short pulse width insures that the sea bottom reflection do not contribute to the surface echo power (Mastrogiuseppe et al., 2014).

The RSR technique constrains surface properties from the stochastic behavior of the amplitude for the surface echo peaks. The technique's principles have been firstly introduced with the Shallow Radar (SHARAD, 20-MHz central frequency, 10-MHz bandwidth) data onboard the Mars Reconnaissance Orbiter (Grima et al., 2012). Then, the RSR has been fully described and demonstrated with the High Capability Radar Sounder (HiCARS, 60-MHz central frequency, 15-MHz bandwidth) airborne radar in Antarctica (Grima et al., 2014a, 2014b, 2016).

In a first step, the signal components P_c and P_n are quantitatively extracted from the surface signal by best-fitting the amplitude (A) distribution of surface echoes for a given region with an Homodyne K-envelope (HK). HK statistics are derived by modeling the scattering with a random walk of negative-binomial statistics (leading to a K-noise) and in which a deterministic (a.k.a. homodyning) component is added (Jakeman and Tough, 1987; Dutt and Greenleaf, 1994). Analytically, the HK distribution is related to the product of a Rice (P_{Ri}) and a gamma (P_Γ) distribution (Jakeman and Tough, 1987):

$$P_{HK}(A|a, s^2, \mu) = \int_0^\infty P_{Ri}(A|a, s^2 w) P_\Gamma(w|\mu, 1) dw \quad (1)$$

where the coherent and incoherent powers are $P_c = a^2$ and $P_n = 2s^2$, respectively, and μ is the scatterer clustering parameter. The HK distribution appears to be the only model for which the parameters keep their physical meaning in the limiting case (Destrempes and Cloutier, 2010). It is a flexible model that does not require the condition of large scatterer number to be fulfilled and allows the scatterers to be clustered (non-stationarity) within the radar footprint. The bin width for an amplitude histogram is determined with the rule from Freedman and Diaconis (1981) that estimates the scale of the distribution from its interquartile range.

In a second step, once P_c and P_n have been deduced from the fit, they are introduced in a backscattering model to assess the surface properties. If the signal can be considered absolutely calibrated (i.e. a perfectly flat conductor would have a fully coherent surface echo amplitude of unity) we have (Grima et al., 2012):

$$P_c = \left|\frac{1-\sqrt{\varepsilon}}{1+\sqrt{\varepsilon}}\right|^2 e^{-(4\pi\sigma_h/\lambda)^2} \quad (2)$$

$$P_n = \frac{2}{h^2}\int_0^r G^2\sigma^\circ x dx \Leftrightarrow P_n = 2\int_0^\vartheta \frac{tan^{-1}(\theta)}{\theta^2+1} G^2\sigma^\circ d\theta \quad (3)$$

where h is the range to the surface, $r = 2\sqrt{hc/B}$ is the radius of the circular pulse-limited footprint from where reflectors could contribute to the scattered part of the received signal and where $B =$

4.25 MHz is the signal bandwidth. The normalized radar cross-section σ^0 (or normalized RCS) is weighted by the 2-way antenna Gain G^2 that varies across the footprint with the incident angle θ (West et al., 2009). By convenience, the right hand of eq. (3) gives P_n as a function of θ after substitution of $x = h\,tan^{-1}(\theta)$ in the left part. $\vartheta = tan(r/h)$ is the maximum incident angle for the considered footprint. To model σ° we use the Integral Equation Model (IEM) as described by Fung et al. (1992), assuming no volume scattering, no multiple scattering, and no shadowing effects (the last two being common at normal incidence) and valid for $\sigma_h < 0.32\lambda$ (7 mm). Then, σ° is function of ε, σ_h, and l_c, making the equation system defined by eqs. (2)–(3) solely dependent on those three unknowns. Noteworthy, we consider a surface of normally distributed heights and with an auto-correlation function exhibiting a Gaussian decline. Although these statistical behaviors can vary with waves formation and growing processes, we consider they could lead to an informative ranges of surface properties.

The relative surface return amplitudes ($0 < A < 1$) are derived from the normalized RCS per burst that are available online through the Planetary Data System[1] (PDS). The later has been obtained by assuming the target as a scatterer illuminated by a beam-limited footprint while, in the specific case of Titan lakes, it is more accurate to consider the target as a reflector. The conversion of the provided normalized RCS to a reflection coefficient A^2 describing the reflector's properties can be obtained from the following reasoning. The basic radar power budget relationship for the total received power is $P = RS/H$, where R is the radar system gain, H is the propagation losses, and S represents the surface losses (e.g. Ulaby and Long, 2014). If the target is considered as a scatterer then $H = 1/(16\pi^2 h^4)$ and $S = A_0\sigma^\circ$ where $A_0 = \pi(h\theta_w/2)^2$ is the beam limited footprint and θ_w is the beamwidth (the considered observations have a beam-limited footprint radius ranging from 24 km to 37 km). In the case of a reflector, $H = 1/(16\pi h^2)$ and $S = A^2$. Substituting those expressions in the radar power budget equation for both the scattering and reflecting case leads to the conversion relationship $A^2 = \frac{\theta_w^2}{4}\sigma^\circ$.

For more stable statistics we increase the number of available observations by considering the surface echo amplitude recorded from each pulses contained within a burst. The pulse amplitudes are absolutely calibrated by adjusting their mean to match the amplitude of the burst.

Lastly, for our technique to be valid, the data need to verify the statistical independence hypothesis for the surface echoes. The signal received at the antenna is the coherent summation of the elementary electromagnetic fields arising from the numerous scatterers within the radar beam-limited footprint. Statistical independence is met if this summation insures randomness of the total energy at the antenna from an acquisition to the next. Because the roughness is also random, the statistical independence is validated when the illuminated area between two pulses do not significantly overlap, but it is not obvious this stands for the Cassini RADAR as consecutive pulses are very close to each other. However, combination of other phenomena could ensure statistical independence by providing a way to vary the phases of the scattered elementary fields at the scale of the RMS heights (few millimeters) such as the range variation to the surface and the dynamic nature of the sea surface. It can be shown that amplitude histograms plotted from non-consecutive echoes do not exhibit a different behavior than those presented in section 3 (Fig. 2). Furthermore, the consistency between our inverted surface properties and other studies (section 4) so that the statistical independence is likely met.

[1] http://pds-imaging.jpl.nasa.gov/volumes/radar.html.

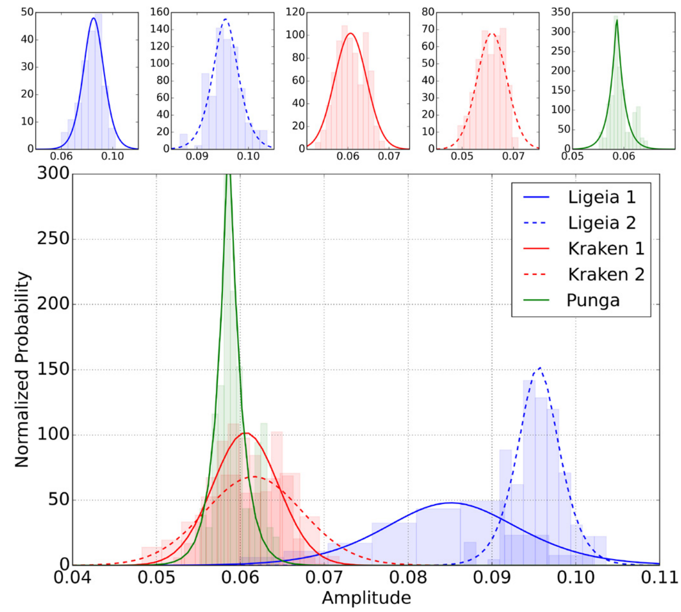

Fig. 2. (Top) Surface echo amplitude histogram for each of the 5 considered regions and its related fit with an HK envelope. x- and y-axis are absolute amplitude and normalized probability, respectively. (Bottom) Overlap of previous plots at same scales for comparison.

3. Results

The amplitude distributions for the surface echoes of each of the five studied regions and the related fit with an HK envelope are shown in Fig. 2. The surface return from Ligeia 1 is characterized by a distinctive stochastic behavior with a larger standard deviation than Ligeia 2. This could be due to the larger incidence angle (> 0.07° degrees) of the Ligeia 1 observations and therefore could start to loose the specular (coherent) return in which case the RSR methodology is less applicable. Although reported in this paper, the surface properties inverted for Ligeia 1 should then be considered with caution. All the other regions of interest have $\theta_o < 0.07°$. Kraken 1 covers the main part of the sea while Kraken 2 crosses a bay, a.k.a. Sinus Moray, further over the same orbit but the two regions exhibit similar statistical distribution. Punga is the latest covered area of the set and its track delineates the larger body of the sea with a narrower bay. Punga has a narrow amplitude distribution along with a high kurtosis usually associated to a very weak incoherent power. The derived signal components from the HK fits are summarizes in Table 1 along with additional observation parameters. In this table, we chose to provide P_c along with the P_c/P_n ratio since, unlike P_n, the later is independent of absolute calibration and contains only the roughness information weighted by the range to surface (contribution of the permittivity is canceled) (Grima et al., 2014b).

According to the IEM and the associated assumptions in the previous section, each $[P_c, P_n]$ pair for a given region is solution of an equation system with three unknowns describing the surface properties $[\varepsilon, \sigma_h, l_c]$. The corresponding field of solutions are plotted on Fig. 3. The surface RMS height, σ_h, increases with surface roughness and is usually related to the wave height by $w_h = 4\sigma_h$ (Holthuijsen, 2010) (i.e., the average of the highest 1/3 of the waves). The correlation length, l_c, is a characteristic horizontal distance beyond which the height of two points can be considered uncorrelated. Hence, the surface roughness increases with decreasing l_c. This is translated in Fig. 3 by the roughest regions lying in the upper-left corner while the smoothest surfaces are on the lower right. On this figure is also indicated the effective slope defined as $s_e = \sigma_h/l_c$, and somewhat related to the more commonly

Table 1
Compilation of observation parameters and RSR-derived results for the five studied locations. Surface roughness parameters are given for methane- ($\varepsilon = 1.73$) and ethane- ($\varepsilon = 2.0$) dominant liquids (Mitchell et al., 2015). Bursts with $\theta_0 > 0.07°$ were not considered, except for Ligeia 1. The same goes for bursts with footprint partially covering land areas, as well as saturated bursts encountered over Kraken 1.

Lake	L_S[a] (°)	Bursts #	θ_0[b] (°)	P_c (dB)	P_c/P_n (dB)	ρ[c] (%)	$\varepsilon = 1.73$		$\varepsilon = 2.0$	
							σ_h (mm)	s_e (°)	σ_h (mm)	s_e (°)
Ligeia 1	45.22	248036884–6929	0.08-0.10	−21.4	16.4	97.0	1.8	0.5	2.1	0.9
Ligeia 2	45.22	248036939–7004	0.04-0.07	−20.4	27.1	93.3	1.5	1.4	1.8	2.3
Kraken 1	59.38	261039902–9997	0.05-0.07	−24.4	20.7	90.7	2.2	1.7	2.5	2.4
Kraken 2	59.38	261040105–0153	0.00-0.06	−24.2	17.2	95.5	2.2	1.1	2.5	1.6
Punga	63.78	265025417–5453	0.02-0.03	−24.6	26.7	87.5	2.3	3.6	2.5	4.9

[a] Solar Longitude.
[b] Pointing angle to normal incidence.
[c] Correlation coefficient of the fit.

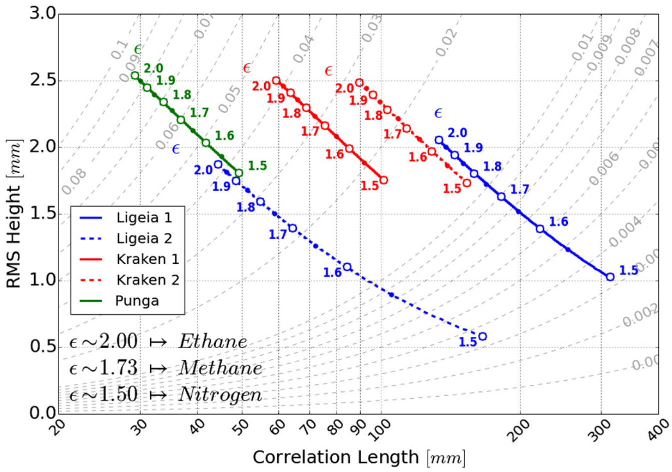

Fig. 3. Ranges of surface properties solutions for Ligeia, Kraken 1, Kraken 2, and Punga. Each solution is a triplet with a specific correlation length (x-axis), RMS height (y-axis), and permittivity (numbers on curves). They are obtained from the IEM applied to the RSR-derived signal components for the Cassini RADAR surface echoes at normal incidence. Dashed-oblique gray lines are the corresponding effective slopes (in radians) assuming similar horizontal scales for the derived RMS heights and correlation lengths.

used RMS slope (Shepard et al., 2001). In this simplistic geometric description the magnitude for the horizontal wavelength of the waves could be estimated as twice l_c.

Whatever the studied region, the surface roughness increases with the considered permittivity for the lake's liquid. Liquid bodies on Titan are believed to be a dominant mixture of ethane ($\epsilon \approx 2.0$) and methane ($\epsilon \approx 1.73$) with possible traces of soluble Nitrogen ($\epsilon \approx 1.5$) (Mastrogiuseppe et al., 2014), so that it is reasonable to restrict the possible permittivity range from 1.73 to 2.0 (Mitchell et al., 2015). At the time of observations, Punga is the rougher surface of the set with permittivity-dependent parameters range of $\sigma_h = 2.3$–2.5 mm (i.e., $w_h = 9.1$–10.1 mm) and $l_c = 30$–36 mm giving an effective slope in the range of $s_e = 3.6$–$4.9°$. Ligeia 2, Kraken 1, and Kraken 2 have similar effective slopes of $s_e = 1.1$–$1.7°$ and $s_e = 1.6$–$2.4°$ for methane- and ethane-dominant composition, respectively. At the time of observations, Kraken mare has RMS heights similar to Punga's and slightly larger than Ligeia (1.5–1.9 mm).

We have considered a model of two semi-infinite media (atmosphere and liquid hydrocarbon) bounded by the surface. In the case of a film thinner than the wavelength covering the sea surface (three-layered model), the permittivities inverted in Fig. 3 would be an effective value varying with the film thickness between the true permittivity of the main liquid body and the one of the overlying film (Mouginot et al., 2009).

4. Discussion and conclusion

Overall, the roughness parameters for Kraken and Ligeia are confined within RMS heights of $\sigma_h = 1.5$–2.5 mm ($w_h = 6.0$–10 mm) and effective slopes of $s_e = 1.1$–$2.4°$. The latter extends up to 3.6–4.9° if the rougher Punga is included. The lower bound of those ranges has to be considered if the composition is methane-dominant as suspected at Ligeia (Mastrogiuseppe et al., 2014, 2016; Mitchell et al., 2015). These RMS heights are consistent with previous radar observations (Wye et al., 2009; Zebker et al., 2014), but the effective slopes are one to two orders of magnitude higher than VIMS single measurements at Jingpo Lacus (Stephan et al., 2010; Barnes et al., 2011). Such slopes associated with millimeter waves correspond to correlation lengths of few meters. Following the IEM, such a surface configuration would led to $P_c/P_n < 1$ (negative in dB scale) corresponding to amplitude distributions of higher skewness and width that we do not observe on Fig. 2 (Destrempes and Cloutier, 2010), suggesting VIMS observations benefited from favorable conditions that produced a highly smooth sea surface. The increase of incoherent energy for a flatter surface is a counterintuitive effect well described by backscattering models in the case of quasi-specular surfaces at normal incidence (Ulaby and Long, 2014). For instance, consider the opposite case of a surface with fixed RMS heights but increasing slopes. It produces the same amount of coherent energy but increasingly scatters the incoherent power off the specular direction. This reduces P_n at normal incidence while the incoherent energy integrated throughout the scattering function is kept consistent. This is well illustrated by Punga, which has both the stronger P_c/P_n ratio and the highest roughness of our dataset.

The Cassini RADAR also produces side-looking images (i.e., off-nadir scattering record). In this mode, the 2.2 cm signal over the lakes has an apparent homogeneity and is weak compared to the surrounding lands (Fig. 1), two characteristics verified by our derived surface properties. Signal homogeneity is explained by the sub-wavelength RMS heights (by one order of magnitude) that cannot generate a fully-developed speckle, while lakes darknesses suggest weak scattering strength at high incidence angles. Indeed, applying the IEM to any surface property configurations obtained in Table 1 shows that the normal radar cross section ($\sigma°$) of the lakes would fall below the instrumental noise floor (about −25 dB) for incident angles larger than 10–30°.

Importantly, the RSR technique needs a lot of surface echoes to infer the signal statistics, and the data acquisition strategy of future planetary radar investigations should consider a large density of echoes matching the scale of the regions of interest. In our case, the RSR-derived surface properties are only representative of the values dominating the sea-scaled portion of tracks shown on Fig. 1. If smaller patches of higher roughness should occur within those tracks, they might not produce enough surface echoes to significantly change the trend of the amplitude distributions (Fig. 2), making them invisible through the RSR process. In the best case, two regions with different but equally-dominant scattering regimes might produce a bi-modal distribution that is not obvious on our measurements. Hence, quiet sea surfaces might be a dominant trend during the northern early summer, but fields of waves activity might occur over local patches and/or might not be sustained over significant periods of time. Then, our measurements are not incompatible with, for example, Earth-like catspaw textures when the wind speed is below the wave generation threshold, localized and/or transient rainfalls, or patches of floating debris. Our measurements are unable to discriminate between those various processes but they constrain the framework for further investigations. For instance consider wind-driven waves for which Hayes et al. (2013) give wavelength thresholds distinguishing capillary (wavelength < 10 mm) from gravity (wavelength > 100 mm) waves, where restoring forces are dominated by surface tension and gravity, respectively. Consider that the wavelength can be approximated by twice l_c (section 3), then our measurements (Fig. 3) are incompatible with capillary waves and would favor gravity waves, except for Punga that falls into the capillary-gravity transition regime.

Acknowledgements

The authors would like to thank the Cassini Radar Science Team for their support and precious suggestions. Grima acknowledges the support of California Institute of Technology Jet Propulsion Laboratory through subcontract 1518949. Portions of this research were carried out at the Jet Propulsion Laboratory, California Institute of Technology, under a contract with the National Aeronautics and Space Administration.

References

Aharonson, O., et al., 2014. Titan's surface geology. In: Muller-Wodarg, I., et al. (Eds.), Titan, pp. 63–101.

Barnes, J.W., Soderblom, J.M., et al., 2011. Wave constraints for Titan's Jingpo Lacus and Kraken Mare from VIMS specular reflection lightcurves. Icarus 211, 722731. http://dx.doi.org/10.1016/j.icarus.2010.09.022.

Barnes, J.W., Sotin, C., et al., 2014. Cassini/VIMS observes rough surfaces on Titan's Punga Mare in specular reflection. Planet. Sci. 3, 3. http://dx.doi.org/10.1186/s13535-014-0003-4.

Bennett, H.E., Porteus, J.O., 1961. Relation between surface roughness and specular reflectance at normal incidence. J. Opt. Soc. Am. 51 (2), 123. http://dx.doi.org/10.1364/J0SA.51.000123.

Destrempes, F., Cloutier, G., 2010. A critical review and uniformized representation of statistical distributions modeling the ultrasound echo envelope. Ultrasound Med. Biol. 36 (7), 1037–1051. http://dx.doi.org/10.1016/j.ultrasmedbio.2010.04.001.

Dutt, V., Greenleaf, J.F., 1994. Ultrasound echo envelope analysis using a homodyned K distribution signal model. Ultrason. Imag. 16 (4), 265–287.

Elachi, C., et al., 2004. Radar: the Cassini Titan radar mapper. Space Sci. Rev. 115, 71–110. http://dx.doi.org/10.1007/s11214-004-1438-9.

Freedman, D., Diaconis, P., 1981. On the histogram as a density estimator: L 2 theory. Z. Wahrscheinlichkeitstheor. Verw. Geb. 57 (4), 453–476. http://dx.doi.org/10.1007/BF01025868.

Fung, A.K., Li, Z., Chen, K.S., 1992. Backscattering from a randomly rough dielectric surface. IEEE Trans. Geosci. Remote Sens. (ISSN 0196-2892) 30, 356–369. http://dx.doi.org/10.1109/36.134085.

Ghafoor, N.A.-L., et al., 2000. Wind-driven surface waves on Titan. J. Geophys. Res., Planets 105 (E5), 12077–12091. http://dx.doi.org/10.1029/1999JE001066.

Grima, C., Kofman, W., et al., 2012. Quantitative analysis of Mars surface radar reflectivity at 20 MHz. Icarus 220, 84. http://dx.doi.org/10.1016/j.icarus.2012.04.017.

Grima, C., Blankenship, D.D., et al., 2014a. Surface slope control on firn density at Thwaites Glacier, West Antarctica: results from airborne radar sounding. Geophys. Res. Lett. 41 (19), 6787–6794. http://dx.doi.org/10.1002/2014GL061635.

Grima, C., Schroeder, D.M., et al., 2014b. Planetary landing-zone reconnaissance using ice-penetrating radar data: concept validation in Antarctica. Planet. Space Sci. 103, 191–204. http://dx.doi.org/10.1016/j.pss.2014.07.018.

Grima, C., Greenbaum, J.S., et al., 2016. Radar detection of the brine extent at McMurdo Ice Shelf, Antarctica, and its control by snow accumulation. Geophys. Res. Lett. http://dx.doi.org/10.1002/2016GL069524.

Hayes, A.G., et al., 2013. Wind driven capillary-gravity waves on Titan's lakes: hard to detect or non-existent? Icarus 225, 403–412. http://dx.doi.org/10.1016/j.icarus.2013.04.

Hofgartner, J.D., Hayes, A.G., Lunine, J.I., Zebker, H., Stiles, B.W., et al., 2014. Transient features in a Titan sea. Nat. Geosci. 7, 493–496. http://dx.doi.org/10.1038/ngeo2190.

Hofgartner, J.D., Hayes, A.G., Lunine, J.I., Zebker, H., Lorenz, R.D., et al., 2016. Titan's "Magic Islands": transient features in a hydrocarbon sea. Icarus 271, 338–349. http://dx.doi.org/10.1016/j.icarus.2016.02.022.

Holthuijsen, L.H., 2010. Waves in Oceanic and Costal Waters. Cambridge University Press.

Jakeman, E., Tough, R.J.A., 1987. Generalized K distribution: a statistical model for weak scattering. J. Opt. Soc. Am. A 4 (9), 1764. http://dx.doi.org/10.1364/JOSAA.4.001764.

Lorenz, R.D., Hayes, A.G., 2012. The growth of wind-waves in Titan's hydrocarbon seas. Icarus 219, 468–475. http://dx.doi.org/10.1016/j.icarus.2012.03.002.

Lorenz, R.D., Kraal, E.R., et al., 2005. Sea-surface wave growth under extraterrestrial atmospheres: preliminary wind tunnel experiments with application to Mars and Titan. Icarus 175, 556–560. http://dx.doi.org/10.1016/j.icarus.2004.11.019.

Lorenz, R.D., Newman, C., Lunine, J.I., 2010. Threshold of wave generation on Titan's lakes and seas: effect of viscosity and implications for Cassini observations. Icarus 207, 932–937. http://dx.doi.org/10.1016/j.icarus.2009.12.004.

Mastrogiuseppe, M., Poggiali, V., et al., 2014. The bathymetry of a Titan sea. Geophys. Res. Lett. 41, 1432–1437. http://dx.doi.org/10.1002/2013GL058618.

Mastrogiuseppe, M., Hayes, A., et al., 2016. Radar sounding using the Cassini Altimeter: waveform modeling and Monte Carlo approach for data inversion of observations of Titan's seas. IEEE Trans. Geosci. Remote Sens. 99, 1–11. http://dx.doi.org/10.1109/TGRS.2016.2563426.

Matson, D.L., Spilker, L.J., Lebreton, J.-P., 2002. The Cassini/Huygens mission to the Saturnian system. Space Sci. Rev. 104, 1–58. http://dx.doi.org/10.1023/A:1023609211620.

Mitchell, K.L., et al., 2015. Laboratory measurements of cryogenic liquid alkane microwave absorptivity and implications for the composition of Ligeia Mare, Titan. Geophys. Res. Lett. 42 (5), 1340–1345. http://dx.doi.org/10.1002/2014GL059475.

Mouginot, J., et al., 2009. MARSIS surface reflectivity of the south residual cap of Mars. Icarus 201, 454. http://dx.doi.org/10.1016/j.icarus.2009.01.009.

Ogilvy, J.A., 1991. Theory of Wave Scattering From Random Rough Surfaces. IOP Publishing Ltd., Bristol, England.

Poggiali, V., et al., 2016. Liquid-filled canyons on Titan. Geophys. Res. Lett. http://dx.doi.org/10.1002/2016GL069679.

Shepard, M.K., et al., 2001. The roughness of natural terrain: a planetary and remote sensing perspective. J. Geophys. Res. 106, 32777–32796. http://dx.doi.org/10.1029/2000JE001429.

Stephan, K., et al., 2010. Specular reflection on Titan: liquids in Kraken mare. Geophys. Res. Lett. 37, L07104. http://dx.doi.org/10.1029/2009GL042312.

Ulaby, F.T., Long, D.G., 2014. Microwave Radar and Radiometric Remote Sensing. The University of Michigan Press.

West, R., et al., 2009. Cassini RADAR sequence planning and instrument performance. IEEE Trans. Geosci. Remote Sens. 47 (6), 1777–1795. http://dx.doi.org/10.1109/TGRS.2008.2007217.

Wye, L.C., Zebker, H.A., Lorenz, R.D., 2009. Smoothness of Titan's Ontario Lacus: constraints from Cassini RADAR specular reflection data. Geophys. Res. Lett. 36 (16). http://dx.doi.org/10.1029/2009GL039588.

Zebker, H., et al., 2014. Surface of Ligeia Mare, Titan, from Cassini altimeter and radiometer analysis. Geophys. Res. Lett. 41, 308–313. http://dx.doi.org/10.1002/2013GL058877.